Drying Process of Sulfide-Based All-Solid-State Battery Components—Investigation on Adhesion Strength and Microstructural Changes

Célestine Singer,* Lorenz Kopp, Milot Aruqaj, and Rüdiger Daub

Sulfide-based all-solid-state batteries are a promising future cell concept to enhance energy densities and create an advantage in safety aspects in comparison to conventional lithium–ion batteries. To guarantee a high performance of the cells, a pronounced interfacial contact between the single components and a homogeneous microstructure is essential to reduce ionic resistances and enhance mechanical stability. To produce sheets on a large scale, established processes such as mixing, coating, drying, and calendering can be applied. The drying process is the most energy consuming and cost-intensive process with major influence on the component's microstructure and mechanical properties. As the latter is of particular importance for industry-relevant manufacturing, this research study focuses on the influence of process and product parameters on prevailing microstructural phenomena and adhesion strength of sulfidic composite cathodes and separators. Results show that the microstructure is changed at temperatures above 50 °C, leading to a significant loss of adhesion strength.

1. Introduction

The sulfide-based all-solid-state battery (ASSB) is a concept for a new generation of battery cell type and consists of solid sheet-type components,[1] which can be produced by adapting conventional processing routes[2] and production environments such as dry rooms.[3] To produce thin-film separators and composite cathodes, wet-coating techniques using doctor blades[4–7] and slot dies followed by convection or infrared drying can be used in the industrial production. However, a major novelty in ASSB production is not only the active material and solid electrolyte but also

C. Singer, L. Kopp
TUMint. Energy Research GmbH
Lichtenbergstr. 8, D-85748 Garching, Germany
E-mail: celestine.singer@iwb.tum.de

C. Singer, L. Kopp, M. Aruqaj, R. Daub
Institute for Machine Tools and Industrial Management
Technical University Munich
Boltzmannstraße 15, D-85748 Garching, Germany

the used solvent, conductive carbon, and binder.[8] Due to the strong reactivity of sulfide-based solid electrolytes in organic solvents, the choice of a suitable solvent for wet processing is restricted to nonpolar and weak polar solvents. The choice of polymeric binder is limited to nitrile-butadiene rubber and ethyl cellulose or styrene-butadiene rubber.[6,7,9] As a result, the limited selection of these materials highly affects the slurry recipes, achievable microstructures, and binder transport mechanism during processing. This has a major influence on the adhesion strength of the coating to the substrate[10] defining process parameters needed for a high-quality ASSB production.

New challenges arise for the fabrication of ASSBs as the ion transport is based on the contact between solid particles not only within one component, such as the composite cathode or the separator, but also at the interface between them.[11,12] These particle contacts need to be well pronounced to counter mechanical stresses arising during industry-relevant roll-to-roll processing and cell cycling.[10,12] In ASSBs, an even higher stress compared with other battery types is induced as the expansion of the cells is characterized by mostly unknown and hardly controllable volume differences of pure lithium metal.[13] In addition to cracks, the complete delamination of components might occur causing an abrupt decrease in ionic and electrical conductivity resulting in a poor cycling stability.[13,14] To improve the cell with regard to the physical contact of single components, the components' adhesion strength is analyzed quantitatively enabling the comparison of mechanical properties of the cell components with the prevailing forces during processing and cycling.

As known from conventional lithium-ion batteries (LIB) manufacturing, various parameters and process-related settings influence the microstructure. However for LIB cathodes and anodes, the behavior of thick films and cracks,[15] convection drying parameters,[16] and delamination behavior[17] were investigated with regard to adhesion and cell performance, these analyses have not been presented for sulfide-based ASSBs so far. Therefore, the question is whether the binder migration, segregation, and diffusion processes shown in LIB electrodes[15,16,18–22] are also existing during the ASSB component processing.

In this work, an experimental setup with an adhesion strength test was built up in Argon atmosphere to quantify the effect of

binder or other particle migration inside sulfide-based ASSB components on the components' adhesion. Already existing studies on adhesion measurements with different tools such as surface and interfacial cutting analysis system,[23] tension and shear-loading tests,[24] peel-off tests, and z-tensile strength tests[10,25–27] were taken as a basis for the investigations. To the best of the authors knowledge, this study is the first to present microstructural effects in correlation with industry-relevant process parameters for sulfide-based ASSB components based on the solid electrolytes Li_6PS_5Cl (LPSCl) and $Li_7P_3S_{11}$ (LPS).

2. Experimental Section

All experiments and tests were conducted in an Argon-filled glovebox (MB 200, MBraun GmbH).

2.1. Mixing

For the sulfidic separator slurry, the $Li_7P_3S_{11}$ (LPS) powder (Solid Ionics Co., Ltd.) was dispersed in a binder solution of 5–7 wt% hydrogenated acrylonitrile-butadiene rubber (HNBR) (Therban LT 1707 VP, Arlanxeo GmbH) dissolved in toluene (99.8%, Sigma-Aldrich GmbH) with solid contents between 30 and 45 wt%. The toluene was dried using a molecular sieve before use. The dispersion was mixed by using the Speedmixer (DAC 1100.2 VAC-P, Hauschild SpeedMixer GmbH) for 20 min at 1000 rpm. The composite cathode was mixed by using the lithium nickel manganese cobalt oxide (NMC622) (BASF Toda Battery Materials AG), LPSCl (Solid Ionics Co., Ltd.), Super C65 (Imerys Graphite & Carbon), and HNBR by a ratio of 67:28:3:2, respectively, and solid contents between 50 and 60 wt%. The binder was dissolved in toluene with a share of 5 wt% before adding the solid components. The cathode slurry was prepared by using the Speedmixer for either 80 min (short-mixing time) or 120 min (long-mixing time) at rotation speeds between 500 and 1600 rpm

in three steps. **Table 1** provides all materials and the respective densities and particle sizes (d_{50}).

2.2. Coating

For thin-film sheet fabrication, the slurry was coated with an automated doctor blade (AB3650, TQC Sheen GmbH) with coating gaps of 150–400 µm on aluminum foil (16 µm) and coating velocities of 1 cm s^{-1}. The coatings with respective mass loadings and porosities are provided in **Table 2**. Various coating gaps were used to provide differing mass loadings. Both values, the mass loading and the porosity, were calculated by weighting and measuring the coating thicknesses.

2.3. Drying

The sheets were either dried at room temperature (RT) (inside the glovebox) at 25 °C for 24 h or between 50 and 100 °C for 5 min in the oven of the glovebox lock (MB-VOH-250, MBraun GmbH) under ambient pressure. Here, 2.9×2.9 cm^2 samples were punched out of the dry sheets with a punching tool (Spahn GmbH& Co. KG). The drying curves were determined by drying the coated sheets at certain temperatures in an Argon-filled glovebox lock. Samples were taken every 30 s and directly weighed. The measurements were repeated at least three times.

2.4. Analysis of Microstructure and Composition

For the analysis of microstructural changes in the powder and sheet-type samples, a scanning electron microscope (SEM) and energy-dispersive X-ray spectroscopy (EDS) (IT 200, Jeol) were used. The samples were analyzed using the secondary electron detector mode with an acceleration voltage of 15 kV and a probe current of 60 µA. Herein, described SEM images were taken from the top view of samples.

2.5. Adhesion Tests

The adhesion tests were conducted with a z-tensile strength test using a uniaxial testing machine (Z020, ZwickRoell GmbH & Co.KG). Furthermore, a compression velocity of 0.75 mm min^{-1}, a dwell time of 30 s, a pull-off velocity of 100 mm min^{-1}, and a data acquisition rate of 2000 Hz were used. The machine was prepared by gluing an adhesive tape (3M, #410 m) on the upper and lower sample holder. A detailed overview on the measurement

Table 1. Densities and particle sizes of the material used for the fabrication of composite cathodes and SESs.

Material	NMC622	LPS	LPSCl	C65	HNBR	Toluene
Density [g cm^{-3}]	4.7	1.98	1.64	1.6	0.96	0.87
Particle size (d_{50})	10.6 µm	3 µm	1 µm	<50 nm (primary particle)	–	–

Table 2. Data of produced solid electrolyte sheets and composite cathodes. Mean values were calculated of all measured samples. A standard deviation of all values is ±10%.

Sample name	Material composition [wt%]	Coating gap [µm]	Sheet thickness (dry) [µm]	Mass loading (dry) [g m^{-2}]	Porosity [%]
LPS/HNBR-5	LPS:HNBR ≈95:5	150	59	37	60
		200	80	55	56
		300	115	80	56
LPS/HNBR-7	LPS:HNBR ≈93:7	200	83	52	59
CC/LPSCl	NMC622:LPSCl: HNBR:C65 ≈68:27:2:3	300	110	120	65
		400	155	208	56

principle and machine set-up is presented in ref. [26] Samples with an area of 6.25 cm² were placed on the sample holder and compressed at a homogeneously distributed contact stress.

The z-tensile strength test allowed multiple parameters to be set to measure the adhesion strength of thin-film samples. Therefore, most of the machine parameters were kept constant (see Figure SA1, Supporting Information A), whereas the most important one, the contact stress, was investigated for the composite cathode and the solid electrolyte sheets separately.

As shown in Figure SA1 (Supporting Information A), the contact stress was varied between 500 and 2500 kPa and the resulting degree of removal (DOR) was analyzed. The DOR describes the area, which was pulled off during testing in relation to the initial area of 6.25 cm². The DOR was analyzed taking picture of the samples and measuring with the program Gimp (GNU image manipulation program). With increasing contact stress, the adhesion strength of both components was rising. At 2500 kPa, there was a high deviation of adhesion strength values resulting in nonvalid measurement results. Out of this reason, a contact stress of 2000 kPa was chosen for both components in every following measurement.

Consequently, the samples were pulled off and the maximum tensile stress was measured at the point of adhesion failure, which was declared as adhesion strength, via a 2.5 kN load cell.

3. Results and Discussion

3.1. Fundamentals of the Drying Process

3.1.1. Microstructure of ASSB Components

The microstructure of ASSB composite cathodes and solid electrolyte separators (SESs) differs from LIB electrodes (**Figure 1**). Slurrys are composed of a binder solution, active material, carbon black, and complemented with solid electrolyte to provide ionic conductivity. Therefore, a variety of particle sizes and different mechanical properties of the single components is present in the slurry resulting in wet and dry sheets. The share of solvent is similar but slightly higher than in LIB slurrys with ≈40–50 wt% depending on the kind of active material, the ratio of active material to solid electrolyte, and binder content. In addition, there is the SES, which contains a solvent share of 50–70 wt% (depending on the particle size of the pristine powder), the sulfide-based electrolyte itself, and the binder. The binder share is typically between 5 and 9 wt% depending on the pristine powder and mechanical flexibility of the sheets.[5] After wet coating of the slurrys, the solvent is evaporating, whereas the sheet shrinks from a wet-film thickness ($t_{wet, C, LIB}$, $t_{wet, C, ASSB}$, $t_{wet, S, ASSB}$) to the final thickness of the dry sheet ($t_{dry, C, LIB}$, $t_{dry, C, ASSB}$, $t_{dry, S, ASSB}$).[21] As shown in Figure 1, the ASSB cathode is of approximately the same thickness or
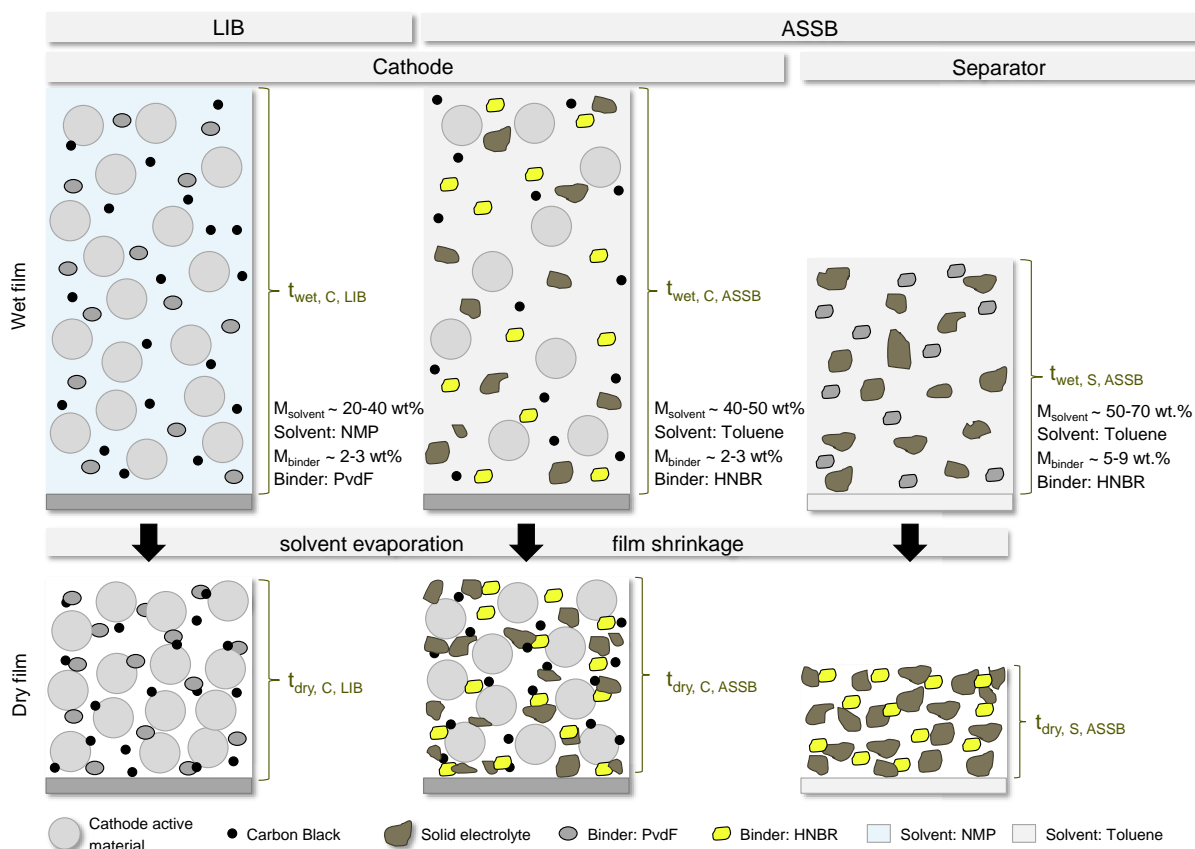

Figure 1. Schematic image of the microstructure, solvent share, binder content, and material choice of ASSB components in comparison to a conventional LIB cathode. The components are compared as wet film and dry film after solvent evaporation and film shrinkage.

ADVANCED
SCIENCE NEWS
www.advancedsciencenews.com

Energy Technology
Generation, Conversion, Storage, Distribution
www.entechnol.de

thicker as an LIB cathode ($t_{dry, C, LIB} = t_{dry, C, ASSB} \approx 70-100\,\mu m$) depending on the targeted energy density and therefore active material share. As ASSB cathodes also inhibit solid electrolyte, the mass loading is dependent on the density of the solid electrolyte. SES needs to be below 50 μm thickness ($t_{dry, S, ASSB}$) (Figure 1) (compaction leads to further decrease and 0% porosity); otherwise, the ASSB cells lose in power and energy density.[28] Table 1 provides an overview of the densities and particle sizes of the materials, which are used to fabricate the composite cathode and the SES.

3.1.2. The Binder System—"HNBR"

As known from several research groups, the drying process has a major impact on the distribution of particles inside the sheets.[15–22,29] Typically, several effects such as evaporation, sedimentation, diffusion, and capillary networks take place during drying. Those cause a particle rearrangement and affect the adhesion and cohesion in cathodes and anodes.[30] Although the cohesion describes the strength between particles inside the sheets, the adhesion characterizes the maximum strength between the sheet and the substrate. Verdier et al.[8] proved that in general HNBR is beneficial over polyvinylidene difluoride (PVdF) in terms of reversible deformation enabling a three times higher adhesion strength than PVdF. In addition, its temperature stability is excellent ranging from −40 to 160 °C.[31] Therefore, thermal stability of the binder is given at the tested drying temperatures and no brittle behavior of the binder is noticed. As shown in Figure SB1a,b) (Supporting Information B), the HNBR binder dissolves fully in toluene and residues are not visible after dissolution even at high magnifications. The LPS solid electrolyte shows a very homogeneous distribution of particles with the same size and shape (see Figure SB1c, Supporting Information) and the binder is well distributed in between (see Figure SB1d, Supporting Information). The formation of capillaries at high porosities inside thin films for such a homogeneous layer is very likely to happen. Moreover, Figure SC1 (Supporting Information C) shows the dependence of a higher adhesion strength with a rising binder share for the LPS system, which proofs the strong correlation of those parameters. An analysis regarding the presence of the known phenomenon of binder migration needs to be conducted.

3.1.3. The Solvent—"Toluene"

Toluene is commonly used as a solvent for sulfide-based ASSB components exhibiting highly different properties compared with N-methyl-2-pyrollidone (NMP) (conventional solvent for LIB cathodes), which are provided in **Table 3**. The properties of toluene differ in terms of molar mass, its boiling point, and especially in the evaporation number. As the evaporation number describes the volatility of the solvent, toluene is sorted to the group of light volatility group of light volatility with a value of 6.1, whereas NMP belongs to the group of very heavy volatility with a value of 95.0. This concludes that toluene is evaporating faster than NMP. In terms of wet coating with solvent shares up to 70 wt%, the sheet fabrication of ASSB components will underlie major differences in the process steps of coating and drying.

Fast evaporating solvents can lead to two phenomena. On the one hand, a faster drying process (higher drying rates) at lower drying temperatures might be possible. On the other hand, an unknown effect on pore development inside the wet coatings may occur because of new materials with different particle sizes and process behavior.[21] To validate material properties of NMP and toluene in experiments, pure solvents were stored to measure their evaporation rate in a glovebox environment. Therefore, Figure SD1 (Supporting Information D) shows the percentage change of solvent mass over a time of 600 s. As shown, the evaporation rate of toluene is significantly higher than for NMP, which results in a reduction of remaining solvent mass of about 7.264% after 600 s. In contrast, the change of NMP mass is only about 0.074%. The respective evaporation rates are $1.0317 \times 10^{-2}\,g\,m^2\,s^{-1}$ for toluene and $2.33 \times 10^{-4}\,g\,m^2\,s^{-1}$ for NMP. The effect of these results on the drying process of ASSB cathodes and solid electrolytes is further investigated in the following.
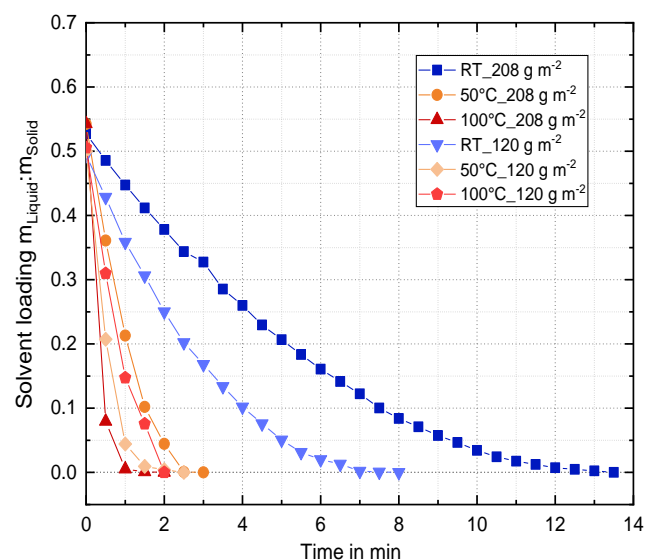
Table 3. Comparison of properties of NMP and toluene as commonly used solvents in a wet-coating process for LIB and ASSB cathodes.[34]

Property	NMP	Toluene
Molar mass	99.13 g mol	92.14 g mol
Boiling point	+203.00 °C	+110.60 °C
Solubility	Miscible with water	Sparingly soluble in water
Explosion limit	1.52–9.5 vol% (air)	1.1–7.1 vol% (air)
Flash point	+86 °C	+4 °C
Ignition point	265 °C	480 °C
Evaporation number	95.00	6.10

Figure 2. Drying curve for CC/LPSCl composite cathodes with mass loadings of 208 and 120 g m^{-2} at RT, 50, and 100 °C.

**ADVANCED
SCIENCE NEWS**
www.advancedsciencenews.com

Energy Technology
Generation, Conversion, Storage, Distribution
www.entechnol.de

3.2. Drying of Composite Cathodes

3.2.1. Drying Curve

To evaluate the behavior of the solvent in wet coatings, drying curves for composite cathodes were measured. **Figure 2** shows the resulting drying curves with the ratio of the liquid mass (m_{Liquid}) to the solid mass (m_{Solid}) presented as solvent loading over time for cathodes with respective mass loadings of 120 g m^{-2} (1.45 mAh cm^{-2}) and 208 g m^{-2} (2.5 mAh cm^{-2}). RT cathodes reached a fully dried state after 8 min (120 g m^{-2}) and 13.5 min (208 g m^{-2}). At 50 °C, the drying time was shortened to 2.5 and 3 min. Increasing the drying temperature to 100 °C results in drying times of 1.5 and 2 min.

As known from literature,[22] temperatures above 120 °C and short-drying times of few seconds lead to the rearrangement of particles and due to capillary forces, light particles are carried to the surface within the coating. Binder particles tend to migrate and, therefore, the adhesion and cohesion might deteriorate. To evaluate the influence of temperature drying with regard to changes in the microstructure of ASSB components, adhesion tests are conducted in the following.

3.2.2. Influence of Mass Loading on Adhesion Strength

The mass loading is one of the most important properties to verify the quality of cathodes and anodes in conventional LIB production. Its value is referring to the amount of active material giving information about the specific capacity and energy density of the cells. Herein, the mass loading of composite cathodes for ASSBs was varied to analyze the influence of this property on the drying behavior and resulting adhesion strength. The adhesion strength is determined as the maximum strength between the
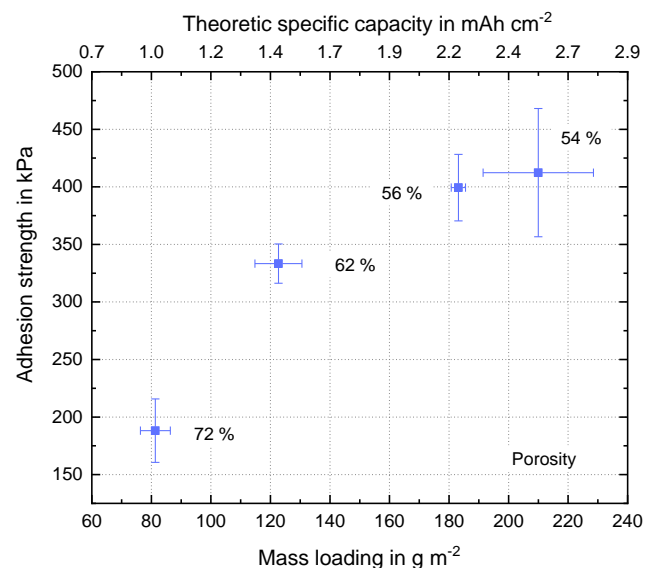
coating and the substrate before a partly or full delamination is occurring.

Therefore, mass loadings were increased from 81 to 210 g m^{-2} with respective specific capacities between 1.02 and 2.55 mAh cm^{-2}. As shown in **Figure 3**, the adhesion strength significantly rises with increasing mass loadings. Samples with an average mass loading of 81 g m^{-2} were delaminated from the aluminum substrate foil with a maximum tension of 188 kPa. An increase in mass loading off about 50% to 123 g m^{-2} brings along a steep growth of adhesion strength up to 333 kPa. For cathode samples with even higher mass loadings of 183 and 210 g m^{-2}, the adhesion test reaches maximum tensions of 400 and 412 kPa. In summary, the data show a steep incline, which correlates with the increase in mass loading. At higher mass loadings, a flattening curve is observed between the data points. In addition to the mass loading or thickness of the sheet, another influencing factor was observed to change. The porosity decreases at higher mass loadings and differs about 18% in the range of samples. A dependence between the mass loading and porosity is therefore revealed.

3.2.3. Influence of Drying Temperature on Adhesion Strength

A detailed analysis was conducted to investigate the influence of the drying temperature and therefore drying rate of the composite cathode samples. As shown in **Figure 4**, a major decrease in adhesion strength is observed with increasing drying temperature. Starting at RT as reference, the cathodes with 208 g m^{-2} mass loading already lose 6% (in average) of their adhesion strength at 50 °C. At 80 and 100 °C, only 64% of the initial adhesion strength remains. The thinner cathodes show a similar behavior but maintain at least 83% of their maximum adhesion strength of 333 kPa. In conclusion, thinner composite cathodes are not as sensitive to high temperature drying than thicker composite cathodes ones.
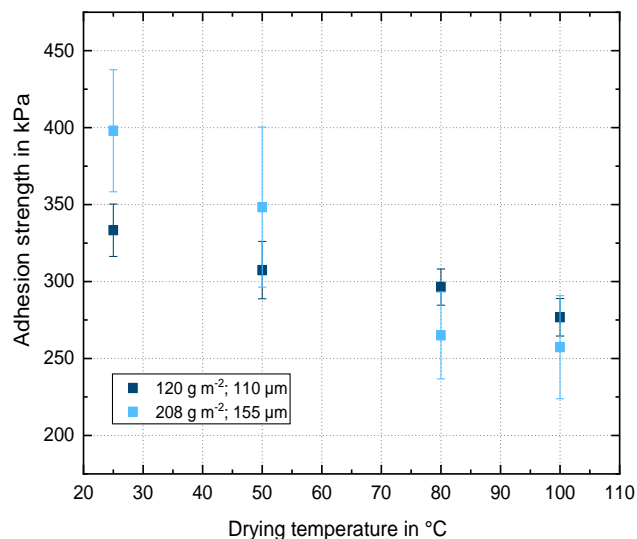

Figure 3. Adhesion strength of composite cathodes (CC/LPSCl) with mass loadings of 81 g m^{-2} (1.02 mA cm^{-2}), 123 g m^{-2} (1.5 mAh cm^{-2}), 183 g m^{-2} (2.23 mAh cm^{-2}), and 210 g m^{-2} (2.55 mAh cm^{-2}). Resulting porosities are between 54% and 72%.

Figure 4. Adhesion strength of composite cathode sheets (CC/LPSCl) as a function of drying temperature. The sheets were dried for 5 min each at the respective temperature. Mass loading of 120 g m^{-2} (110 μm sheet thickness) and 208 g m^{-2} (155 μm sheet thickness) was tested.
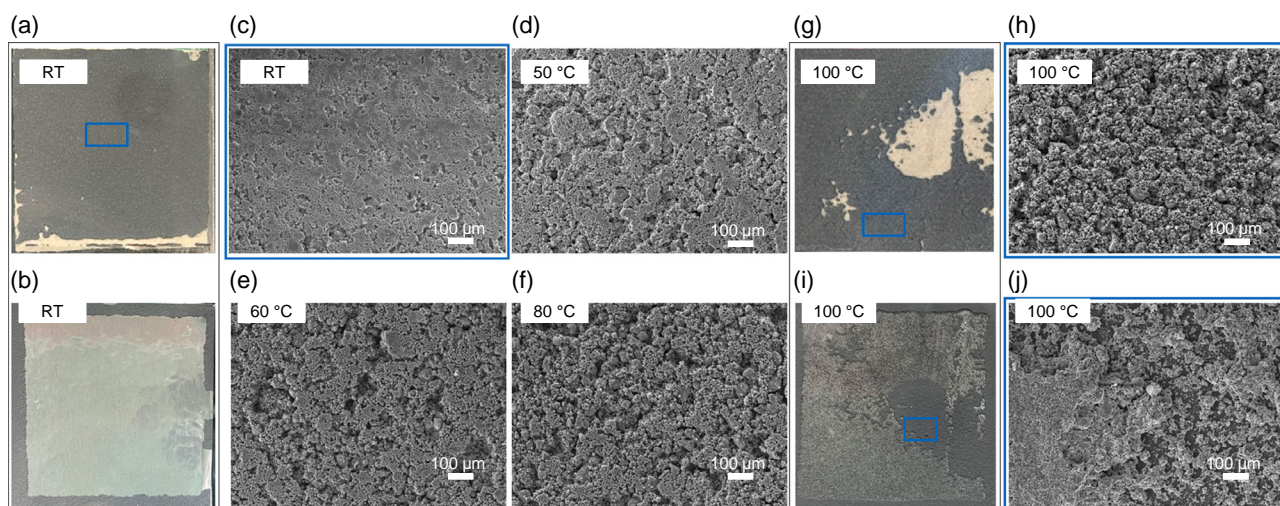
Figure 5. Upper: Pictures and SEM images of composite cathodes samples after adhesion test. a,b) Pictures of the upper and lower part of RT sample after testing. A clear adhesion failure between sample and substrate is visualized; c–f) SEM images of samples dried at RT, 50, 60, and 80 °C. g–j) Pictures and SEM images of the upper and lower part of sample after testing. Major residues are left on the aluminum substrate. The SEM images show the delaminated parts of the cathodes, which are in contact with the adhesive tape.

Pictures and SEM images of the composite cathode samples after testing are shown in **Figure 5**. As for RT samples as well as 50 and 60 °C samples, the aluminum appears in a clear silver surface after delaminating the samples (Figure 5b), the adhesion failure was found to be predominant as failure mechanism. The delaminated parts of the coatings are visualized in SEM images showing a clear trend toward greater pores with higher temperatures (Figure 5c–f). These give a hint on residues, which were broken out of the sheets and are left over on the aluminum. At temperatures above 80 °C major residues of the cathode can be found on the delaminated aluminum (cf. Figure 5g,i). Figure 5h,j shows the respective SEM images of porous and destroyed surfaces for both the upper and lower part of the sample. EDS

analysis of the surface does not show any significant increase in the C amount, which is inside HNBR and the conductive additive. Nevertheless, the adhesion strength shows that a major particle movement is taking place.

3.3. Drying of the SES

3.3.1. Drying Curve

The same measurements were conducted for the LPS separator sheet. **Figure 6** shows longer drying times at RT than the composite cathode. Solid electrolytes with mass loadings of 55 g m^{-2} are fully dried after 13.5 min, whereas sheets with 80 g m^{-2} need 16 min until end of solvent evaporation. Increasing the temperature to 50 °C, drying times can be significantly reduced to 2.5 min and, at a temperature of 100 °C, all samples are dried after 30 s. An increase in temperature from 25 to 50 °C shortens the drying time by about 70–80%. At 100 °C, the drying time is reduced by more than 90%. Although the beginning of every curve tends to show a linear decline of the solvent loading, the inclination decreases toward the end of the drying process. With regard to the existing drying theories and explanations of LIB electrodes' drying behavior, this result shows a diminishing presence of capillary transport as dominating effect.[15,30] The higher drying times for the solid electrolyte in comparison to the composite cathode at RT are emphasizing the assumption of a dominating pore emptying effect instead of capillary forces favoring a quicker solvent evaporation.[15,30]

Although composite cathodes consist of a heterogeneous microstructure with large active material particles and small solid electrolyte particles, the solid electrolyte has a homogeneous structure with one particle type. The porosities are in the same range for both components, whereas the mass loading and sheet thickness are higher for the composite cathodes (see Table 2). Therefore, the drying process at RT might be repressed for SES due to smaller pores. Despite, at higher temperatures, the drying process of solid electrolytes is
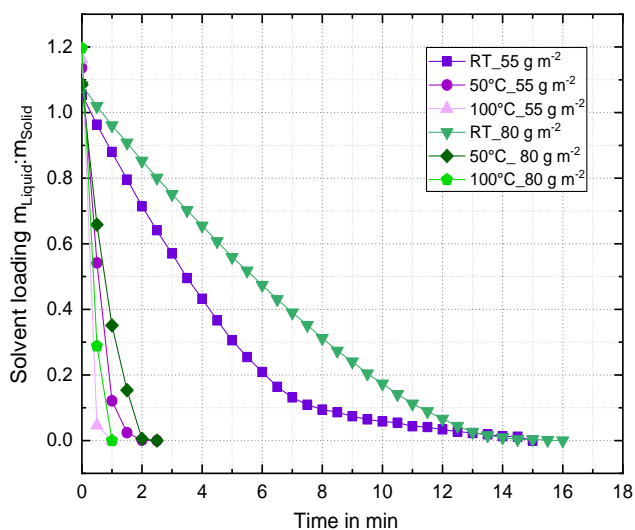

Figure 6. Drying curve for LPS/HNBR-5 solid electrolyte sheets with mass loadings of 55 and 80 g m^{-2} at RT, 50, and 100 °C.
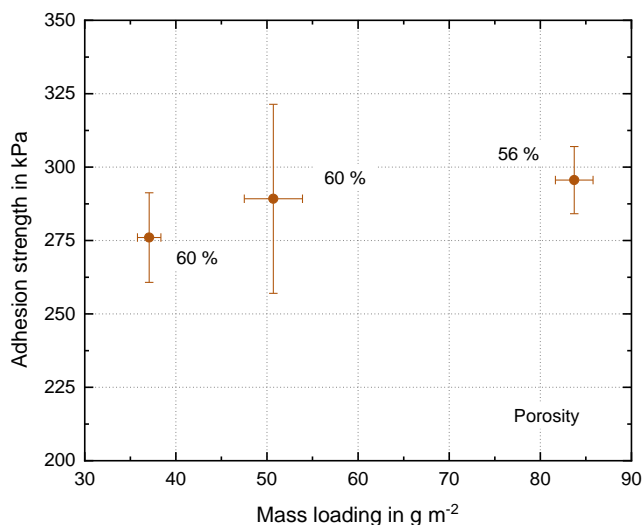
Figure 7. Adhesion strength of solid electrolyte sheets (LPS/HNBR–5) with mass loadings of 37, 51, and 84 g m^{-2} and porosities between 56% and 60%. Sheet thicknesses: 37 g m^{-2} ≈59 μm (coating gap: 150 μm), 51 g m^{-2} ≈77 μm (coating gap: 200 μm), and 84 g m^{-2} ≈120 μm (coating gap: 300 μm).

Figure 8. Adhesion strength of solid electrolyte sheets (LPS/HNBR–5) as a function of the drying temperature. The sheets were dried for 5 min at the respective temperature. Mass loadings of 55 g m^{-2} (80 μm sheet thickness) and 80 g m^{-2} (115 μm sheet thickness) were tested.

faster leading to the assumption that drying at elevated temperatures forces a capillary transportation. The drying rate of the remaining solvent will depend on the properties of the solvent, in this case toluene, and the pore sizes. Here, especially the mass transfer coefficient will determine the velocity of the drying process. A high porosity and a large pore size would accelerate this process.

3.3.2. Influence of Mass Loading on Adhesion Strength

As a second variation, the influence of different mass loadings on the adhesion strength was investigated. The respective mass loadings of 37, 51, and 84 g m^{-2} were tested after drying at RT for 24 h. As shown in **Figure 7**, the two lighter samples show results in the same range of ≈276–289 kPa, whereas the highest mass loading also shows the highest adhesion strength with 296 kPa. A trend can be assumed by the average values, but the deviation of all three sample types is high. Nevertheless, the porosity of the sheets seems to change with higher coating gaps. Therefore, a lower porosity might be an influential factor on the adhesion strength. The same effect, but not as pronounced, was stated previously for the composite cathode (see Figure 3).

3.3.3. Influence of Drying Temperature on Adhesion Strength

The influence of the drying temperature on the respective adhesion strength was analyzed by a variation of drying temperatures for the solid electrolyte sheets. **Figure 8** shows a steep decline of the adhesion strength for the dried samples in comparison to the RT sample. The 80 μm thick samples show a maximum average adhesion strength of 289 kPa at RT. This value decreases by 44% at a drying temperature of 100 °C down to an average of 163 kPa. The effect is stronger for the 115 μm thick samples, where the
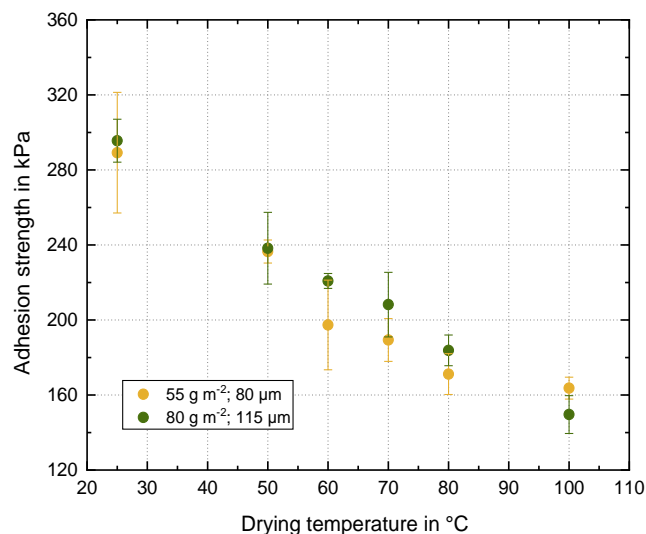
adhesion strength loses about 50% between RT (296 kPa) and 100 °C (150 kPa).

As shown in Figure SE1 (Supporting Information), samples that were dried at RT do not show any significant residues on the aluminum substrate (l). The surface of the delaminated sheet is even (k, m). In contrast, a sample dried at 100 °C exhibits major residues on the top of the aluminum (o, p) and a partly broken structure at the upper part of the sample (n). As shown in
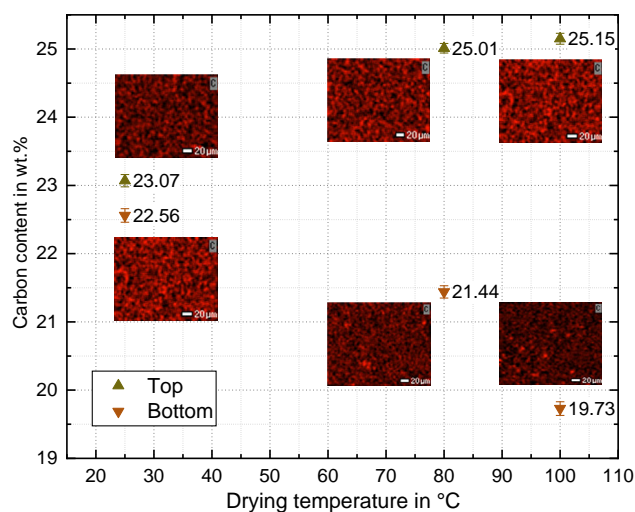

Figure 9. Carbon content over drying temperature of LPS samples measured with EDS analysis in relation to other sample components. A comparison between the carbon at the top and the bottom (facing the aluminum substrate) of the sample is made. An increasing carbon content is observed at the top, whereas the value at the bottom decreases. EDS pictures are showing a qualitative course of the number of pixels correlating with the analyzed mass percentage.

2300098 (7 of 10)

Figure SE1r,s, Supporting Information, the EDS analysis visualizes residues of carbon and sulfur, which indicate the presence of HNBR and LPS on the aluminum. For all solid electrolyte sheet samples, a cohesion failure was recognized at temperatures above 80 °C. Hence, drying temperatures have to be carefully chosen in industrial processing. To evaluate these observations, EDS analyses were conducted. As shown in **Figure 9**, the carbon content (referring to the carbon in the binder HNBR) is increasing at the top of the LPS samples, whereas at the bottom, values are decreasing. Although the qualitative analysis by EDS shows only deviation by ≈2 wt%, the EDS maps also show a correlating number of red pixels, indicating the concentration of carbon.

4. Comparison to LIB

In conclusion, the presented analyses show results, which stay in contrast to those of LIBs. Therefore, different hypotheses for the present phenomena are elaborated in the following and an outlook toward the industrial drying process for ASSB components is given.

4.1. Influence of Mass Loading

Comparing these results to conventional LIB cathodes with similar composition and solid contents, the maximum adhesion strengths are in the same range. A major difference is hence that the mass loadings herein are higher, almost doubled, because the cathode contains additional solid electrolyte and sheet thicknesses rise. To gain equal energy densities, same shares of active material need to be mixed into the composite cathode leading to similar specific capacities while mass loadings increase. Nevertheless, for example, Westphal et al.[21] found out that the adhesion strength for higher mass loadings was decreasing instead of rising. The same observation was made in several more publications.[10,15,21,22,26] Assumptions on influencing factors for a different behavior of ASSB components are summarized in the following: 1) Porosity of the sheets: A higher coating gap results in a less porous sheet due to lower shear rates. High shear rates seem to provoke a break up of particle cohesion resulting in more or larger pores. The homogeneity of particles and particle bonds inside the thinner sheets may be worse. A lower porosity can lead to a better cohesion between the particles and less space where particle can separate from each other; 2) Drying rate: At a constant temperature, the drying process is more time intensive, the thicker the sheets are. A lower porosity even reinforces this as the drying time for low-porosity sheets is higher than for high-porosity sheets. On the one hand, this can result in more time for the particles and the binder to sink toward the substrate during a sedimentation process. On the other hand, larger pores lead to higher drying rates because the evaporation behavior of toluene determines the end of the drying phase. With higher drying rates, more particles are brought to the surface due to capillary effects and therefore are missing at the interface to the substrate; and 3) Particle size: According to Jaiser et al.,[21] smaller particles lead to higher drying times. The LPSCl possesses a d_{50} of ≈1 µm (see Table 1). In contrast, the NMC622 particles have a d_{50} of ≈10.6 µm. For this reason, the microstructure differs majorly

from those of LIB cathodes and the particle arrangement inside the composite cathode sheets might proceed differently.

The correlation between the adhesion strength and the porosity of LIB electrodes was already discussed in literature[25,32] but addressed by calendering. The influence calendering on the adhesion strength was therein shown to play a major role for very dense samples. Between 45% and 55% porosity no major influence was shown. At porosities down to 20–30%, a significant increase in the adhesion strength was proven in Billot et al.,[25] whereas Meyer et al.[32] noticed a decreasing adhesion strength for lower porosities. Their explanation was the introduction of additional forces, for example, shear forces during calendering.

In summary, no clear trend of increasing or decreasing adhesion strength was observed for lower porosities in the past and was also only investigated inducing porosity by calendering. As the particle structure of the composite cathode is more diverse and the present particle types and materials are varying from conventional LIB electrodes, it can be concluded that the relationships shown so far for the LIB cathodes are not transferable to the ASSB components.

4.2. Influence of Drying Temperature

Similar results were shown for LIB electrodes, where higher mass loadings and higher drying temperatures also showed a higher segregation of inactive material.[16] Despite, LIB electrodes usually get dried by applying different temperature profiles, because certain temperatures were found to be beneficial for a higher adhesion strength.[21,33] In this case, no higher temperature than RT was found to bring advantages such as a back diffusion of binder particles toward the substrate. Furthermore, samples of the same thickness of SES and the composite cathodes were compared (115 µm thick SES and 110 µm thick composite cathodes). Here, it becomes clear that the microstructure of the solid electrolyte tends to change more heavily during high-temperature drying. Moreover, the data in Figure 4 and 7 show that thicker samples are stronger influenced by high-temperature drying than thinner samples as losses in the adhesion strength are higher for the first.

5. Conclusion

In summary, the drying behavior and influence of different drying temperatures on the microstructural changes and particle rearrangement inside SES sheets and composite cathodes were analyzed and discussed. The drying curves of both, the solid electrolyte sheets and the composite cathode, show a linear decline in the beginning, which indicates a constant drying rate. At the end of the drying process, the drying rate is decreasing. These analyzes show that the drying processes of those components are not dominated by capillary effects over the whole process. Instead, the solvent and the pore sizes play a major role regarding drying times. When applying higher temperatures, the capillary effect is predominant. This is also shown in decreasing adhesion strengths for higher temperatures. The LPS solid electrolyte sheets and composite cathodes show the expected result of increasing adhesion strength with higher binder amounts and a decreasing adhesion strength for higher drying temperatures and rates. In contrast to

the convention LIB electrodes, a higher mass loading leads to increasing adhesion strength for both components.

All of the samples show an adhesion failure at a drying temperature below 80 °C and a cohesion failure for drying temperatures above this threshold. In comparison to LIB electrodes, a reduced drying temperature is therefore recommended to keep the influence on microstructural changes inside the components as low as possible. In addition, a well-sorted temperature profile can be helpful to control the drying process and prohibit major particle rearrangement. Especially for thick solid electrolyte coatings, a carefully chosen drying process in the industrial production of ASSB components needs to be applied. A first outlook on implications for the industrial drying process is given to enable the planning of production plants and give an initial set of drying parameters for more detailed process studies. Further investigations on the adhesion of the compound of SE and composite cathode as well as film shrinkage behavior and the influence of different solid electrolytes on the drying process are recommended to complete the process studies.

Supporting Information

Supporting Information is available from the Wiley Online Library or from the author.

Acknowledgements

Conflict of Interest

The authors declare no conflict of interest.

Data Availability Statement

The data that support the findings of this study are available from the corresponding author upon reasonable request.

Keywords

[1] K. J. Kim, M. Balaish, M. Wadaguchi, L. Kong, J. L. M. Rupp, *Adv. Energy Mater.* **2021**, *11*, 2002689.

[2] J. Schnell, T. Günther, T. Knoche, C. Vieider, L. Köhler, A. Just, M. Keller, S. Passerini, G. Reinhart, *J. Power Sources* **2018**, *382*, 160.

[3] a) C. Singer, H.-C. Töpper, T. Kutsch, R. Schuster, R. Koerver, R. Daub, *ACS Appl. Mater. Interfaces* **2022**, *14*, 24245; b) C. Singer, H.-C. Töpper, F. J. Günter, G. Reinhart, *Procedia CIRP* **2021**, *104*, 56; c) Y.-T. Chen, M. A. T. Marple, D. H. S. Tan, S.-Y. Ham, B. Sayahpour, W.-K. Li, H. Yang, J. B. Lee, H. J. Hah, E. A. Wu, J.-M. Doux, J. Jang, P. Ridley, A. Cronk, G. Deysher, Z. Chen, Y. S. Meng, *J. Mater. Chem. A* **2022**, *10*, 7155.

[4] a) Y. J. Nam, S.-J. Cho, D. Y. Oh, J.-M. Lim, S. Y. Kim, J. H. Song, Y.-G. Lee, S.-Y. Lee, Y. S. Jung, *Nano Lett.* **2015**, *15*, 3317; b) D. Y. Oh, Y. J. Nam, K. H. Park, S. H. Jung, K. T. Kim, A. R. Ha, Y. S. Jung, *Adv. Energy Mater.* **2019**, *9*, 1802927.

[5] N. Riphaus, P. Strobl, B. Stiaszny, M. Y. Zinkevich, J. Schnell, S. Indris, H. A. Gasteiger, S. J. Sedlmaier, *J. Electrochem. Soc.* **2018**, *165*, A3993.

[6] Y. J. Nam, D. Y. Oh, S. H. Jung, Y. S. Jung, *J. Power Sources* **2018**, *375*, 93.

[7] S. Ito, S. Fujiki, T. Yamada, Y. Aihara, Y. Park, T. Y. Kim, S.-W. Baek, J.-M. Lee, S. Doo, N. Machida, *J. Power Sources* **2014**, *248*, 943.

[8] N. Verdier, S. El Khakani, D. Lepage, A. Prébé, D. Aymé-Perrot, M. Dollé, D. Rochefort, *J. Power Sources* **2019**, *440*, 227111.

[9] a) K. H. Park, D. Y. Oh, Y. E. Choi, Y. J. Nam, L. Han, J.-Y. Kim, H. Xin, F. Lin, S. M. Oh, Y. S. Jung, *Adv. Mater.* **2016**, *28*, 1874; b) J. Zhang, H. Zhong, C. Zheng, Y. Xia, C. Liang, H. Huang, Y. Gan, X. Tao, W. Zhang, *J. Power Sources* **2018**, *391*, 73; c) A. Banerjee, K. H. Park, J. W. Heo, Y. J. Nam, C. K. Moon, S. M. Oh, S.-T. Hong, Y. S. Jung, *Angew. Chem.* **2016**, *55*, 9634.

[10] N. Billot, M. Beyer, N. Koch, C. Ihle, G. Reinhart, *J. Manuf. Syst.* **2021**, *58*, 131.

[11] a) Y.-S. Hu, *Nat. Energy* **2016**, *1*, 1; b) K. J. Kim, M. Balaish, M. Wadaguchi, L. Kong, J. L. M. Rupp, *Adv. Energy Mater.* **2021**, *11*, 2002689.

[12] T. Famprikis, P. Canepa, J. A. Dawson, M. S. Islam, C. Masquelier, *Nat. Mater.* **2019**, *18*, 1278.

[13] R. Koerver, W. Zhang, L. de Biasi, S. Schweidler, A. O. Kondrakov, S. Kolling, T. Brezesinski, P. Hartmann, W. G. Zeier, J. Janek, *Energy Environ. Sci.* **2018**, *11*, 2142.

[14] a) W. Zhang, D. Schröder, T. Arlt, I. Manke, R. Koerver, R. Pinedo, D. A. Weber, J. Sann, W. G. Zeier, J. Janek, *J. Mater. Chem. A* **2017**, *5*, 9929; b) R. Koerver, I. Aygün, T. Leichtweiß, C. Dietrich, W. Zhang, J. O. Binder, P. Hartmann, W. G. Zeier, J. Janek, *Chem. Mater.* **2017**, *29*, 5574; c) G. Bucci, B. Talamini, A. Renuka Balakrishna, Y.-M. Chiang, W. C. Carter, *Phys. Rev. Mater.* **2018**, *2*, 105407.

[15] J. Kumberg, M. Müller, R. Diehm, S. Spiegel, C. Wachsmann, W. Bauer, P. Scharfer, W. Schabel, *Energy Technol.* **2019**, *7*, 1900722.

[16] B. Westphal, H. Bockholt, A. Kwade, *Meet. Abstr.* **2014**, *MA2014-02*, 328.

[17] M. Baunach, S. Jaiser, S. Schmelzle, H. Nirschl, P. Scharfer, W. Schabel, *Drying Technol.* **2016**, *34*, 462.

[18] F. Font, B. Protas, G. Richardson, J. M. Foster, *J. Power Sources* **2018**, *393*, 177.

[19] S. Lim, K. H. Ahn, M. Yamamura, *Langmuir* **2013**, *29*, 8233.

[20] M. Müller, L. Pfaffmann, S. Jaiser, M. Baunach, V. Trouillet, F. Scheiba, P. Scharfer, W. Schabel, W. Bauer, *J. Power Sources* **2017**, *340*, 1.

[21] S. Jaiser, M. Müller, M. Baunach, W. Bauer, P. Scharfer, W. Schabel, *J. Power Sources* **2016**, *318*, 210.

[22] B. G. Westphal, A. Kwade, *J. Energy Storage* **2018**, *18*, 509.

[23] B. Son, M.-H. Ryou, J. Choi, T. Lee, H. K. Yu, J. H. Kim, Y. M. Lee, *ACS Appl. Mater. Interfaces* **2014**, *6*, 526.

[24] H. Luo, J. Zhu, E. Sahraei, Y. Xia, *RSC Adv.* **2018**, *8*, 3996.

[25] N. Billot, T. Günther, D. Schreiner, R. Stahl, J. Kranner, M. Beyer, G. Reinhart, *Energy Technol.* **2020**, *8*, 1801136.

[26] W. Haselrieder, B. Westphal, H. Bockholt, A. Diener, S. Höft, A. Kwade, *Int. J. Adhes. Adhes.* **2015**, *60*, 1.

**ADVANCED
SCIENCE NEWS**

www.advancedsciencenews.com

Energy Technology
Generation, Conversion, Storage, Distribution

www.entechnol.de

[27] H. Jeon, I. Cho, H. Jo, K. Kim, M.-H. Ryou, Y. M. Lee, *RSC Adv.* **2017**, *7*, 35681.

[28] J. Betz, G. Bieker, P. Meister, T. Placke, M. Winter, R. Schmuch, *Adv. Energy Mater.* **2019**, *9*, 1803170.

[29] J. Lee, S. Kim, C. Lee, *Int. J. Precis. Eng. Manuf. Green Technol.* **2019**, *6*, 723.

[30] S. Jaiser, L. Funk, M. Baunach, P. Scharfer, W. Schabel, *J. Colloid Interface Sci.* **2017**, *494*, 22.

[31] L. Valentini, M. A. L. Manchado, *High-Performance Elastomeric Materials Reinforced by Nano-Carbons. Multifunctional Properties And Industrial Applications*, Elsevier, Amsterdam; Oxford; Cambridge, MA **2020**.

[32] C. Meyer, M. Weyhe, W. Haselrieder, A. Kwade, *Energy Technol.* **2020**, *8*, 1900175.

[33] S. Jaiser, A. Friske, M. Baunach, P. Scharfer, W. Schabel, *Drying Technol.* **2017**, *35*, 1266.

[34] *VDI-Wärmeatlas. Mit 320 Tabellen*, Springer Vieweg, Berlin **2013**.